Earth and Planetary Science Letters 369–370 (2013) 305–316

Contents lists available at SciVerse ScienceDirect

Earth and Planetary Science Letters

journal homepage: www.elsevier.com/locate/epsl

Current stress and strain-rate fields across the Dead Sea Fault System: Constraints from seismological data and GPS observations

Mimmo Palano [a,*], Paola Impresciа [b,1], Stefano Gresta [b]

[a] Istituto Nazionale di Geofisica e Vulcanologia, Osservatorio Etneo—Sezione di Catania, Piazza Roma, 2, 95123 Catania, Italy
[b] Dipartimento di Scienze Biologiche, Geologiche e Ambientali—Università degli Studi di Catania, Italy

ARTICLE INFO

Article history:
Received 25 October 2012
Received in revised form
20 March 2013
Accepted 24 March 2013
Editor: P. Shearer
Available online 22 April 2013

Keywords:
focal mechanisms
stress
GPS
strain-rate
Dead Sea Fault System

ABSTRACT

The stress and strain-rate fields characterizing the Dead Sea Fault System are investigated by using seismological and geodetic observations. In order to assess spatial variations in the regional stress field, we compiled a multidisciplinary dataset of well-constrained horizontal indicators, by merging all available data reported in literature with the data obtained in this study through weighted stress inversions of focal plane solutions. Our findings indicate that the state of stress is characterized by the coexistence of a normal faulting stress regime with the primarily strike-slip one, according to the regional frame illustrated by previous geological and seismological observations. An updated velocity field computed from new observations and earlier published data depicts the general left-lateral motion of the Dead Sea Fault System well. In agreement with previous studies, we detected some differences in the slip-rate pattern between the northern and the southern sectors of the fault system. The geodetic strain-rate field highlights how much of the deformation is accommodated along the fault system itself in a narrow region. The comparison between the stress and the strain-rate directions reveals that both orientations are near-parallel, clearly indicating that present-day crustal stress and ground deformation patterns are chiefly driven by the same tectonic processes.

1. Introduction

The Dead Sea Fault System (DSFS; Fig. 1) represents the left-lateral transform boundary between the Arabian plate and the Sinai sub-plate (*e.g.* Eyal et al., 1981; Garfunkel, 1997), stretching from the Red Sea mid-oceanic ridge in the south, to the Bitlis–Zagros (southern Turkey) continental collision zone in the north, where it joins with the East Anatolian fault (EAF). The DSFS formed during the Early-Miocene when the Oligocene–Early Miocene rifting of Arabia and Africa along the Red Sea shifted into the Gulf of Aqaba (Bartov et al., 1980; Garfunkel, 1981; Le Pichon and Gaulier, 1988). Along the northern margin of Arabia, terminal suturing with Asia and closing of the Bitlis–Zagros suture occurred *ca.* 15 Myr (Hempton, 1987), coinciding with basin inversion along the Palmyride Fold belt (PFB; Chaimov et al., 1990). The DSFS propagated from the Gulf of Aqaba to the north encompassing the pre-existing PFB through bending to the east and splaying into several faults.

Most research carried out on the DSFS has focused both on the historical and archaeological seismic history (*e.g.* Ambraseys et al., 1994; Ambraseys and Jackson, 1998; Ellenblum et al., 1998; Klinger et al., 2000; Marco et al., 2005; Sbeinati et al., 2005; Agnon et al., 2006; Elias et al., 2007) and on the estimation of the long-term geological slip-rate (*e.g.* Quennell, 1958; Freund et al., 1970; Ginat et al., 1998; Klinger et al., 2000; Niemi et al., 2001; Gomez et al., 2003; Daëron et al., 2004; Ferry et al., 2007; Makovsky et al., 2008; Searle et al., 2010). GPS measurements undertaken in the area since 1996 have allowed estimating the geodetic slip-rate of discrete segments of DSFS (*e.g.* Mahmoud et al., 2005; Reilinger et al., 2006; Gomez et al., 2007; Le Beon et al., 2008; Alchalbi et al., 2010; ArRajehi et al., 2010; Al Tarazi et al., 2011; Sadeh et al., 2012) evidencing a general agreement with the range of long-term slip-rate estimations from geological observations.

Conversely, few studies have focused on the current tectonic stress field of the DSFS by analyzing earthquake focal mechanisms and fault slip data collected and examined only on specific regions of interest (Lunina et al., 2005; Janssen et al., 2007; Hofstetter et al., 2007). However, the increase over recent decades in geodetic observations of crustal deformation, as well as earthquake recordings, allows considerably improving the understanding of the current state of crustal stress–strain along this plate boundary.

Taking into account new geodetic and seismological observations, we investigated the pattern of the present-day crustal tectonic stress and strain-rate fields characterizing the entire DSFS. We compiled a database of fault plane solutions (FPSs) by merging

* Corresponding author. Tel.: +39 095 7165800.
E-mail address: mimmo.palano@ct.ingv.it (M. Palano).
[1] Now at: Istituto di Geologia Ambientale e Geoingegneria—Consiglio Nazionale delle Ricerche, Rome, Italy.

0012-821X/$ - see front matter © 2013 Elsevier B.V. All rights reserved.
http://dx.doi.org/10.1016/j.epsl.2013.03.043

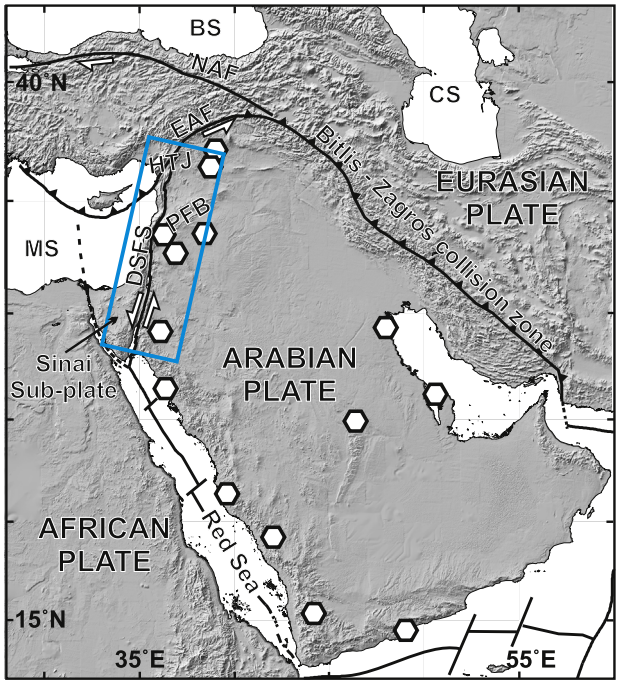

Fig. 1. Regional plate tectonic setting of the study region and surrounding areas. GPS sites used to estimate the Euler vector for the fixed Arabian plate are reported as white hexagons (see Table S2 of the "Supplementary material" section for details). Abbreviations are as follows: BS, Black Sea; CS, Caspian Sea; NAF; North Anatolian fault; ESF, East Anatolian fault; HTJ, Hatay triple junction; MS, Mediterranean Sea; DSFS, Dead Sea Fault System; and PFB, Palmyride Fold belt. Box is showing the study area.

data from public catalogues and literature. Subsequently, we applied a stress inversion analysis to specific subsets to estimate the directions of the three principal stress axes. To improve the spatial density of the stress field, we compiled a multidisciplinary dataset of 27 well-constrained horizontal stress indicators, by including all available data reported in literature and in the World Stress Map project (http://dc-app3-14.gfz-potsdam.de). In addition, we analyzed new GPS data coming from recent continuously operating stations, which were rigorously integrated with published velocities in order to provide a more complete picture of the crustal deformation along the entire DSFS. As a final step, we compared the horizontal directions of compressive stress (from seismological and geological observations) with those of the minimum contractional geodetic strain-rate.

Both geodetic and seismological observations allow to identify discrete deformation domains, mainly involving both strike-slip and extension and generally consistent with the regional frame illustrated by geological data published in literature. Moreover, the comparison between the stress and the strain-rate directions reveals that both orientations are near-parallel, and that, over a large portion of the investigated area, these directions are aligned to the expected Eurasia–Arabia relative motion, showing that the plate-driving forces related to this convergence provide the largest component of the observed strain/stress fields. In the northern sector of the DSFS, this picture is complicated by a complex tectonic interaction between different micro-plates and blocks.

2. Background setting

The DSFS is an approximately 1000 km long left-lateral fault zone and is generally subdivided into three sections (Fig. 2a).

The southern section, extending from the Gulf of Aqaba (Red Sea) through the Dead Sea and the Jordan Valley, is characterized by the presence of predominantly left-lateral strike-slip faults striking between N12°E and N20°E. The 160-km-long Wadi-Araba fault, running NNE from the northern end of the Gulf of Aqaba, represents the longest segment of the southern section of DSFS. This fault encompasses a ~20 km wide depressed zone representing the morphological expression of diffuse faulting within the array. Northward, through the Dead Sea, the Wadi-Araba fault is connected to the left-lateral strike-slip Jordan Valley fault segment. About 40 km north of the Dead Sea, the NW–SE trending left-lateral transtensional Carmel fault segment branches out from the Jordan Valley fault segment and runs to the Mediterranean Sea (Fig. 2a; Garfunkel, 1981).

The central section of DSFS is characterized by the presence of a *ca.* 200-km-long NNE–SSW striking restraining bend, running through Lebanon and SW Syria where the DSFS splays into distinct fault branches. The major branch, called the Yammouneh fault, connects the southern and northern parts of the DSFS, while the other branches connect at about 45° the DSFS with the PFB (Fig. 2a; Garfunkel, 1981; Walley, 1988; Girdler, 1990). The PFB is a NE-trending 400 by 120 km transpressive belt stretching across central Syria; the southern sector of this belt consists of a series of narrow, en echelon, asymmetric folds with an SE vergence cored by predominantly reverse faults while the north-eastern sector (usually divided into two main structural domains) is characterized by the presence of larger-wavelength anticlines and prevailing NE–SW trending strike-slip faults (see Chaimov et al. (1990) for additional details).

The northern section of the DSFS is characterized by the presence of two distinct N–S striking faults bounding the 70-km-long Ghab Valley and intersecting through a complex braided fault system with the EAF and the Cyprus arc (Fig. 2a; Gomez et al., 2003; Karabacak and Altunel, 2013; Meghraoui et al., 2011). This intersection corresponds to the Hatay "fault–fault–trench" triple junction that forms the plate boundaries between Arabia, Africa and Anatolia (Mahmoud et al., 2013).

A total left-lateral slip of 105 km, taking place in two main phases, has been documented along the southern segment of DSFS. About 60 km of displacement was accrued during the Miocene, while about 45 km was accrued from the Pliocene to the present (Bartov et al., 1980; Garfunkel, 1981). Conversely, the northern segment of the DSFS apparently shows considerably less displacement (5.3–16.8 km in the last 3.7 Myr; Searle et al., 2010) with respect to the southern segment. The discrepancy between the displacement along the northern and southern sectors of the DSFS seems puzzling, since the PFB accounts for only 20 km by folding and thrusting shortening (Chaimov et al., 1990).

The occurrence of several large earthquakes (with magnitude $M \geq 7$) in the last 1000 yr along the DSFS is well documented in the historical records (Fig. 2a; Ambraseys and Jackson, 1998; Klinger et al., 2000; Sbeinati et al., 2005). In particular, these records document the occurrence of eight large earthquakes in the northern sector of DSFS, between the Ghab Valley and the Kara Su Valley (AD 1157, AD 1170, AD 1404, AD 1407, AD 1408, AD 1626, AD 1822 and AD 1872; Ambraseys and Jackson, 1998; Sbeinati et al., 2005), three events in its central sector (AD 1202, AD 1759 and AD 1837; Ambraseys and Jackson, 1998) and five events in its southern sector (AD 1033, AD 1068, AD 1212, AD 1293 and AD 1458; Klinger et al., 2000). Since the beginning of instrumental seismicity, the DSFS experienced only one large earthquake ($M = 7.2$; star in Fig. 2a) that occurred in the Gulf of Aqaba on November 22, 1995 (Klinger et al., 2000). In addition, the lack of adequate documentation, due to population density and/or the political situation in the area over much of the last 1000 yr, can reflect bias to magnitude estimation of earthquakes, as for instance in AD

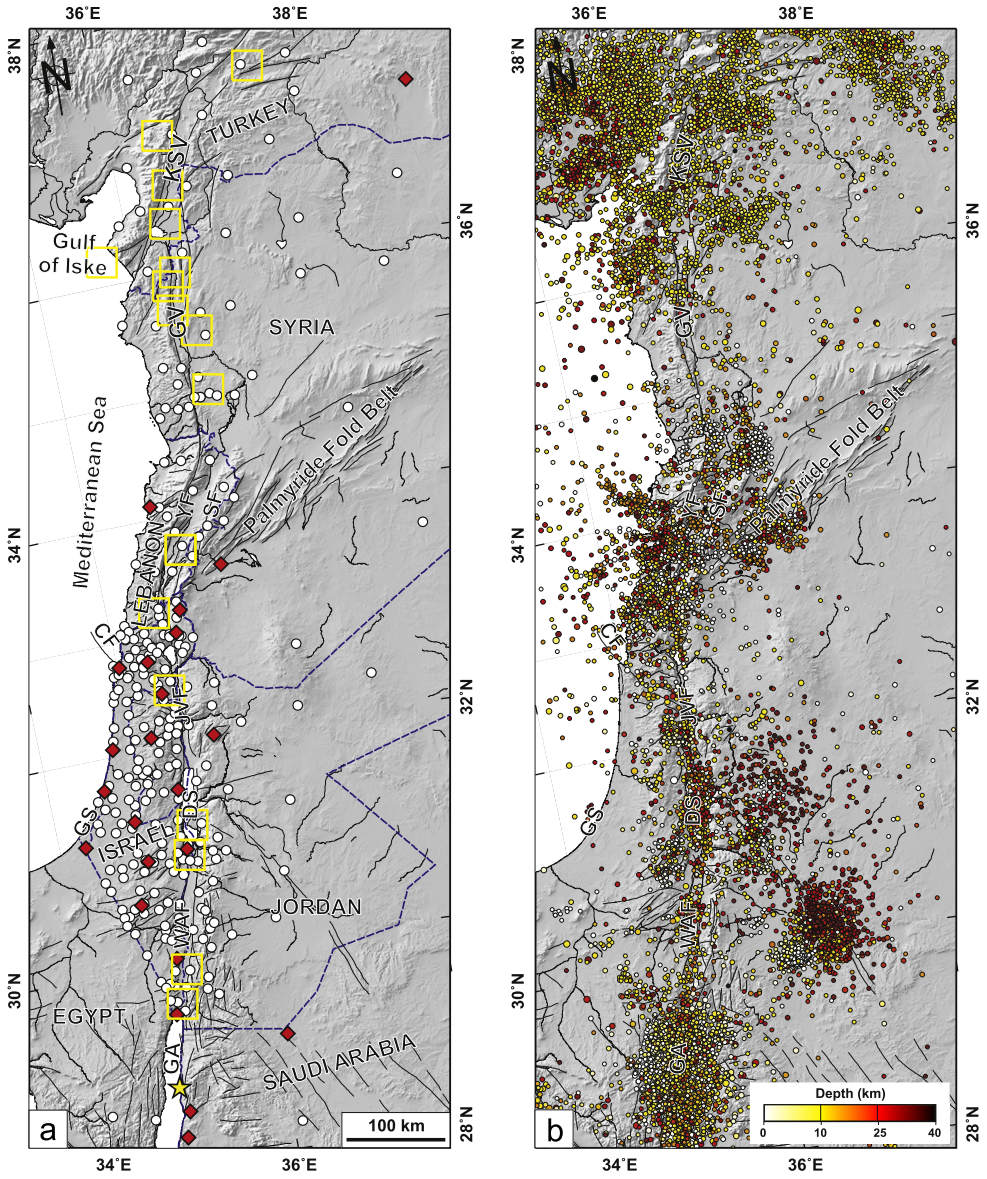

Fig. 2. (a) Simplified tectonic map of the study region. Thick lines denote major faults. Dashed blue lines denote political boundaries. GPS sites used in this work are reported as follows: red diamonds indicate continuous GPS sites processed in this study, and white circles GPS data published by other authors (see Table S2 of the "Supplementary Material" section for details). Yellow squares are historical earthquakes with $M \geq 7$ occurring in the last 1000 yr (Ambraseys and Jackson, 1998; Klinger et al., 2000; Sbeinati et al., 2005). Abbreviations are as follows: KSV, Kara Su Valley; GV, Ghab Valley; YF, Yammouneh fault; SF, Serghaya fault; CF, Carmel fault; JVF, Jordan Valley fault; DS, Dead Sea; WAF, Wadi-Araba fault; and GA, Gulf of Aqaba. (b) Instrumental crustal seismicity ($M \geq 2.6$) occurring in the investigated area since 1980 (http://www.isc.ac.uk). (For interpretation of the references to colour in this figure legend, the reader is referred to the web version of this article.)

1312, AD 1588 and AD 1712 that could have a larger magnitude than the current catalogue estimation (Agnon Amotz, personal communication). Despite the occurrence of these large historical earthquakes, seismic monitoring of the region began in the early 20th century with the establishment of a few seismological stations and around 1980 with the setting up of some continuous operating regional seismological networks (Weber et al., 2009 and references therein). From the International Seismological Centre (http://www.isc.ac.uk) on-line catalogue, we compiled more than 40,000 seismic events (from 1904 to date) having $M \geq 1.5$ and focal depths in the 0–40 km interval. Taking into account all earthquakes having $M \geq 2.6$, we computed a cumulative frequency plot of the depth-distribution of instrumental seismicity. The value of 2.6, usually defined as magnitude of completeness, represents the lowest magnitude for which the catalogue can be considered complete (see Appendix A in the "Supplementary material" section for additional details). This plot shows that 90% of earthquakes occur in the upper crust at depth less than 22 km (see Appendix A in the "Supplementary material" section for additional details), in accordance with results achieved by Aldersons et al. (2003) and Shamir (2006) from relocation of events occurring in the southern sector of DSFS and beneath the Dead Sea region, respectively. Along the DSFS, instrumental seismicity (Fig. 2b) is not uniformly distributed, but is concentrated into three main regions. The northernmost region, including the northern sector of DSFS and the southern part of EAF, is characterized by widespread moderate-level seismicity which well depicts the complex nature of the DSFS–EAF tectonic interaction. During the investigated time interval, this region underwent 12 earthquakes with $M \geq 5.0$. The central section of DSFS, where it joins with the PFB, is also characterized by widespread seismicity, while on the eastern part of PFB the instrumental seismicity decreases. In the studied time span, only two earthquakes with $M \geq 5.0$ took place. Southward, the Gulf of Aqaba area is

characterized by a moderate seismic release with the occurrence of eight earthquakes with $M \geq 5.0$. Here, seismicity is clustered in a continuous 50-km-wide belt following the NNE–SSW attitude of the Gulf of Aqaba. Around the Dead Sea area and along the Jordan Valley fault segment, minor clusters, characterized by events with moderate magnitude (only five earthquakes with $M \geq 5.0$ have occurred in this area during the last 100 yr), can be recognized.

3. Focal mechanisms: data and stress tensor computation

To study the seismic deformation pattern and draw up a detailed map of stress orientations, we have compiled a database of FPSs by merging data from public catalogues and literature. As a first step, we selected focal mechanisms from the following moment tensor catalogues:

- Global Centroid Moment Tensor catalogue (GCMT; http://www.globalcmt.org), which compiles FPSs of earthquakes with $M \geq 5.5$ occurring worldwide since 1976.
- European–Mediterranean Regional Centroid Moment Tensor catalogue of the Istituto Nazionale di Geofisica e Vulcanologia (RCMT; Pondrelli et al., 2011 and references therein; Imprescia et al., 2012; http://www.bo.ingv.it/RCMT/searchRCMT.html), with earthquakes since 1997 and $M \geq 4.5$.
- Eidgenössische Technische Hochschule of Zurich catalogue (ETHZ; Braunmiller et al., 2002, http://www.seismo.ethz.ch/prod/tensors/index), with events with $M \geq 4.5$ and occurring from 1999 to 2006.

To extend the dataset back in time and enlarge the magnitude range, we used published FPSs collected in the "Earthquake Mechanisms of the Mediterranean Area" database (EMMA; Vannucci and Gasperini, 2003, 2004; Vannucci et al., 2010 and references therein; Imprescia, 2010), which contains more than 12,000 FPSs in the Mediterranean area since 1905 and published until 2007 in the last version (3.1). EMMA contains literature FPSs computed through traditional methods (*e.g.* first-motion polarity, S-wave polarization) that have been checked for consistency regarding orientation and orthogonality of nodal planes, corrected for misprints, re-computed and completed with solution parameters when necessary and possible. In addition, to bring our dataset up to date we searched published papers which contain recent FPSs (Abdul-Wahed and Al-Tahhan, 2010; Elenean et al., 2009; Hofstetter et al., 2007; Kraeva et al., 2010). The final dataset includes 239 FPSs (with $M \geq 3$) of which 52 moment tensors are from on-line catalogues (CMT, RCMT, ETHZ), 108 from the EMMA (3.1 version) database and 79 from recently published studies (see Table S1 of the "Supplementary material" section for direct references and additional details). To visualize the proportions of thrust, normal and strike-slip FPSs among the earthquakes in our dataset, we adopted the ternary diagram introduced by Frohlich (1992). This diagram provides a quick and manageable way to determine the dominant style of faulting in a particular region. Fig. 3 reports the distribution of FPSs belonging to our final dataset in the diagram. The distribution of FPSs in the ternary diagram clusters into the left part of the diagram, which corresponds to a mix of strike-slip (40.6%), normal faulting mechanisms (29.7%) and predominantly normal faulting with strike-slip components (5.4%). Some FPSs fall into the lower right part of the diagram, which corresponds to thrust faulting (6.7%) and to predominantly thrust with strike-slip components (0.8%). The remaining 16.7% are considered undefined since they fall into the lower central part of the diagram (defined as "odd" earthquakes by Frohlich (1992)).

The distribution of FPSs along the DSFS indicates that seismic release is predominantly dominated by strike-slip and normal faulting mechanisms (Fig. 4a), highlighting how the two different faulting regimes coexist along the fault system. A few reverse FPSs

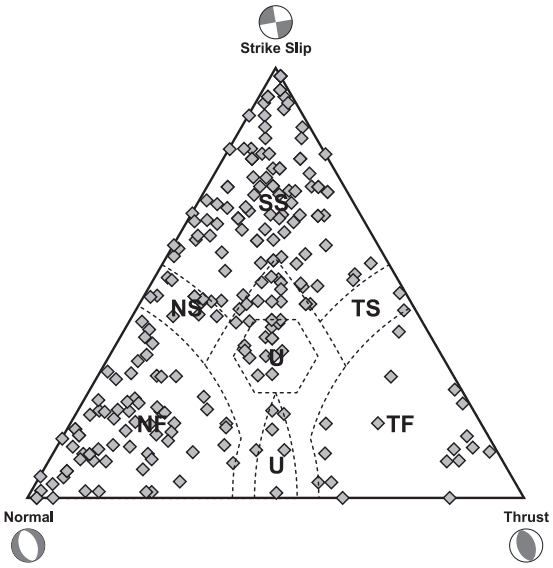

Fig. 3. Ternary plot of focal mechanism data: each point is plotted based on the plunge of the P, T, and B axes of the FPS (Frohlich, 1992). The dashed lines divide the diagram into faulting styles based on definitions by Zoback (1992): NF is normal faulting, NS is normal and strike-slip, SS is strike-slip, TS is thrust and strike-slip, TF is thrust faulting, and U is undefined.

can be recognized in the Gulf of Aqaba and in the north. While the occurrence of earthquakes with reverse faulting mechanism in the northern part of the investigated area can be related to the complex tectonic setting of the Hatay triple junction, it seems surprising in the Gulf of Aqaba region due to the transtensional geometry of the plate boundary. These earthquakes belong to the aftershock sequence following the $M = 7.2$ Gulf of Aqaba earthquake (November 22, 1995; star in Fig. 2a) and nucleated on E–W-oriented faults related to the main Eilat fault (see Hofstetter et al. (2003) for additional details).

The compiled FPSs dataset was inverted to estimate the regional stress tensors. The reliability of each FPS used in the computation is one of the main issues in calculating the state of stress. So, in order to give priority to the most reliable mechanisms, the FPSs were weighted with respect to the quality of the solutions. We therefore assigned a weight (W) to each FPS according to

$$W = C + Ma + Y$$

where C represents the weight related to the kind of solutions. Since moment tensor solutions are generally more stable than traditional ones (*i.e.* first-motion P-wave focal mechanisms) because of determination methods (Arvidsson et al., 1998; Dziewonski and Woodhouse, 1983; Dziewonski et al., 1981), we assigned the largest weights to the moment tensor solutions. In particular, we adopted values of 3, 2 and 1 for moment tensor solutions, for the EMMA database focal mechanisms and for solutions from recent published papers (which were not submitted to EMMA check procedures) obtained with traditional methods, respectively. Ma represents the magnitude value of the corresponding shock. We assigned the largest weights to the events with highest magnitudes since generally (i) small events often exhibit a large scatter due to local structure and stress perturbations and are poorly representative of the regional stress field and (ii) the greater the magnitude, the better the seismogram trace and the higher number of seismic stations registering the event, allowing an improved location and a more reliable FPS determination. In detail, we assigned values of 3, 2 and 1 for FPSs having magnitude $M > 5.5$, $4.5 \leq M \leq 5.5$ and $M < 4.5$, respectively. Y represents the year the earthquakes occurred. Since (i) first

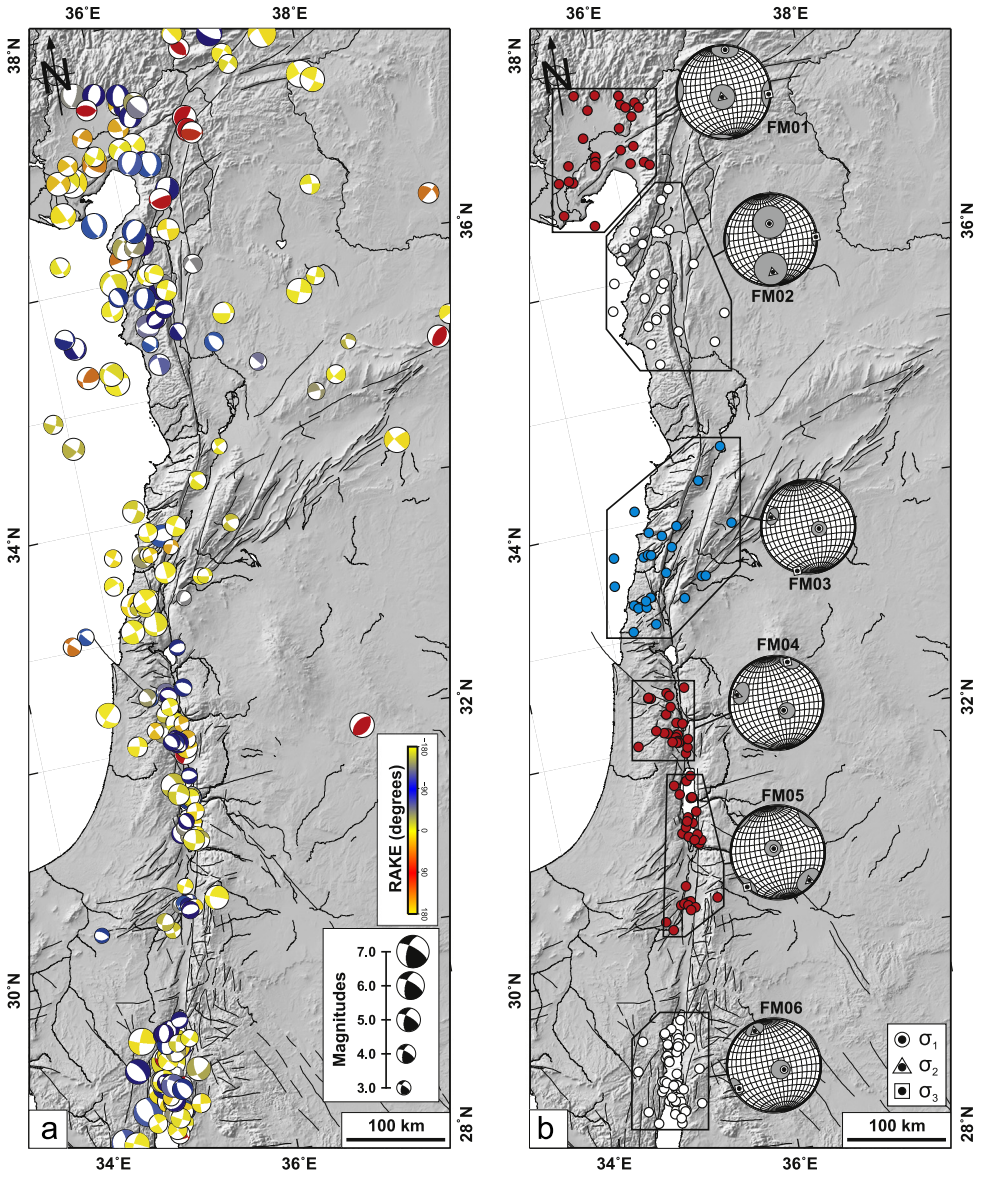

Fig. 4. (a) Lower hemisphere, equal area projection for the 239 FPSs compiled for this study with magnitudes of between 3.0 and 7.2; FPSs are coloured according to rake: red indicates pure thrust faulting, blue is pure normal faulting, and yellow is strike-slip faulting. (b) Location of the 6 selected subsets and graphic output of the stress tensor inversion results. (For interpretation of the references to colour in this figure legend, the reader is referred to the web version of this article.)

moment tensor determinations started in 1976 (digital recording of seismic traces) and (ii) during the 80s and 90s seismic stations improved the recording quality and number and (iii) the use of the regional centroid moment tensor method for earthquakes with moderate magnitude began globally from 1997, we assigned values of 3, 2 and 1 to earthquakes taking place from 1997 to the present, to earthquakes occurring during the 1977–1996 period and to earthquakes occurring before 1976, respectively. According to the above mentioned parameter, W values range from 3 (lower weight) to 9 (higher weight). Taking into account the natural clustering of the events along the DSFS, we selected 6 subsets from sampling the entire DSFS (Fig. 4b). By using the WinTENSOR program (Delvaux and Sperner, 2003) and following the approach described in Delvaux and Barth (2010), we inverted the FPSs to determine the principal stress axes $\sigma1 \geq \sigma2 \geq \sigma3$ and the dimensionless stress ratio R ($\sigma2-\sigma3/\sigma1-\sigma3$), which expresses the magnitude of $\sigma2$ relative to the magnitudes of $\sigma1$ and $\sigma3$. According to the Wallace–Bott hypothesis (Bott, 1959), we assumed the stress field to be uniform and invariant in space and time and that earthquake slip occurs in the direction of maximum shear stress. Computation of the standard deviations was based on the examination of all possible reduced stress tensors for a particular optimal stress solution obtained from the inversion of FPSs. They were defined by combining the possible values of each individual stress axis ($\sigma1$, $\sigma2$, $\sigma3$) and the stress ratio R. For each possible reduced tensor, the horizontal stress directions (S_{Hmax}/S_{hmin}) were computed and the related standard deviations determined (Delvaux, 2012). Subsets and graphic output of the stress tensor inversion results are shown in Fig. 4b and in Table 2. The stress tensor inversion for the 6 selected subsets yields well-constrained principal stress directions and R values (only subset FM02 showed a larger uncertainty, since the inverted dataset contains heterogeneous FPSs). For all subsets the $\sigma3$ is always sub-horizontal (dip values of $\sigma3$ are in the range 0–11°; see Table 2 for details). Subsets FM02, FM03, FM04, FM05 and FM06 are characterized by a normal faulting regime; for these subsets the estimated R values are generally high ($R \geq 0.78$), evidencing that $\sigma2$ and $\sigma1$ may be of similar magnitude. Subset FM01 is characterized by a strike-slip faulting regime ($R=0.63$). It is worth noting that the state of stress of southern DSFS was previously investigated by Hofstetter et al.

Table 1
GPS-Euler vector and associated errors (95% of confidence) for the fixed Arabian plate. The pole was estimated by using the following GPS sites: SOLA MKLA NAMA SANA JEDD HRRN ALWJ UDMC KUWT HALY RSHD BAHR DBSS KBDD (these sites are mapped in Fig. 1).

Plate	Latitude N°	Longitude E°	Ω (deg Myr^{-1})	Error ellipse		Azimuth
				σ_{max}	σ_{min}	
Arabia	50.388 ± 0.134	1.596 ± 0.505	0.577 ± 0.005	1.67	0.20	57.1

Table 2
Stress tensor parameters as obtained from the inversion of the FPSs for each selected dataset. Subsets and graphic output of the stress tensor inversions results are reported in Fig. 4b.

Dataset	σ1 (pl./az.)	σ2 (pl./az.)	σ3 (pl./az.)	R (σ2−σ3/σ1−σ3)	Stress regime	S_{Hmax}	Quality
FM01	09/014	81/213	03/105	0.63	SS	14	B
FM02	61/007	29/189	01/099	0.92	NF	9	C
FM03	71/113	19/296	01/206	0.98	NF	116	B
FM04	72/148	15/294	09/027	0.74	NF	118	B
FM05	80/324	10/144	00/234	0.78	NF	144	B
FM06	71/125	16/343	11/249	0.84	NF	159	B

(2007) through the analyses of a subset of 78 events ($1.1 \leq M \leq 4.1$) occurring from 1987 to 1996. Subsets FM04 and FM05 overlap with the areas investigated by these authors. While for subset FM05 we obtained similar results to those obtained by Hofstetter et al. (2007) (σ1, σ2 and σ3 show very similar orientations and their confidence regions partially overlap), for subset FM04 we obtained different results. In particular, for this subset our solution is characterized by a sub-horizontal σ3 (a plunge of 9° with a normal faulting regime; $R=0.74$) while the solution obtained by Hofstetter et al. (2007) is characterized by an inclined σ3 (plunge is ~40–45° with a strike-slip faulting regime). The reason for this difference may likely be related to the different datasets used to investigate the state of stress on this area (*e.g.* data number, magnitudes and weight associated to each FPS during the inversion procedure). In particular, as mentioned above, Hofstetter et al. (2007) have used a dataset that could be affected by a scatter due to local structure and stress perturbations since a large portion of events (~64%) is characterized by $M < 3.0$. Beside these local differences, both results clearly indicate that $\sigma 2 \approx \sigma 1$, highlighting the tendency of the normal faulting toward the primarily strike-slip faulting stress regime according to the geological transtensional nature of DSFS (Garfunkel, 1981; Salamon et al., 2003).

4. GPS data: network, processing and results

Data acquired by continuous GPS stations installed across the DSFS (Fig. 2a) and freely available at on-line archives (*i.e.* SOPAC, UNAVCO) were processed by using the GAMIT/GLOBK software (Herring et al., 2010) following the strategy described in Palano et al. (2011). To improve the overall configuration of the network and tie the regional observations to an external global reference frame, data coming from 10 continuously operating IGS stations (KUWT, YIBL, SOLA, JEDD, NAMA, ALWJ, NICO, NSSP, PHLW and ZECK; see Table S2 of the "Supplementary material" section for details) were introduced in the processing. By using the GLOBK module, the regional observations are then combined, on a daily basis, with global solutions computed by the SOPAC and aligned to the ITRF2008 reference frame through a seven-parameter Helmert transformation (3 translations, 3 rotations and a scale factor). The resulting time-series were analyzed and corrected for their noise properties, linear velocities, periodic signals, antenna jumps and outliers, according to the strategy described in Nikolaidis (2002). We then combined the corrected daily position estimates and their full covariance matrices to compute a long-term average site velocity in the ITRF2008 reference frame.

Our GPS network shares some stations with those processed by Reilinger et al. (2006), Le Beon et al. (2008), Alchalbi et al. (2010), ArRajehi et al. (2010), Al Tarazi et al. (2011), Sadeh et al. (2012) and Mahmoud et al. (2013) allowing for a rigorous integration of the eight estimated velocity fields. To this end, we aligned the published velocities to the ITRF2008 reference frame by applying a seven-parameter Helmert transformation, obtained by finding the transformation that minimizes the RMS of differences between velocities of common sites. The average discrepancies are small, and the RMS for the 4–13 common stations is less than 0.7 mm/yr. The resulting velocity field and additional details are reported in the "Supplementary material" section. In the following analysis we excluded the velocity field reported in Mahmoud et al. (2013) due to their short observation period. To better show the transcurrent nature of DSFS, the velocity field needs to be referred to an adequate reference frame. The Euler vector components (latitude and longitude of pole, rotation rate) for the Arabian rigid plate were thus estimated by minimizing, with a weighted least squares inversion (Palano et al., 2010), the adjustments to horizontal ITRF2008 velocities of 11 sites within the stable Arabian plate (see Table S2 of the "Supplementary material" section). Most of the residuals are lower than 1 mm/yr. Estimated Euler vectors (Table 1) are then used to rotate the ITRF2008 solutions into the fixed Arabian frame (Fig. 5a).

The resulting velocity field clearly depicts the general left-lateral motion of the DSFS (Fig. 5a). In detail, the velocity field shows an N–S decreasing gradient passing from the higher values (*ca.* 7.5 mm/yr) observed along the Kara Su Valley (where the DSFS joins with the EAF and the Bitlis–Zagros collision zone) to smaller GPS velocity values (*ca.* 1.8 mm/yr) at the southern end of the Ghab Valley. Southward, the area comprised between the PFB and the Gulf of Aqaba is characterized by a gradual increase in velocity values (at a rate of ~0.07 mm/yr per km), passing from values of ~2.9 mm/yr south of PFB to ~5.0 mm/yr close to the Gulf of Aqaba. In general, the deformation field appears to be confined in a narrow area across the DSFS, but two areas characterized by a widespread deformation field can be recognized (Fig. 5). The former comprises the area of the Hatay triple junction, where an E–W divergent gradient is coupled to the N–S convergent one. The latter can be recognized on the western part of the PFB (Fig. 5), where the general left-lateral motion is partitioned into different branches of the DSFS.

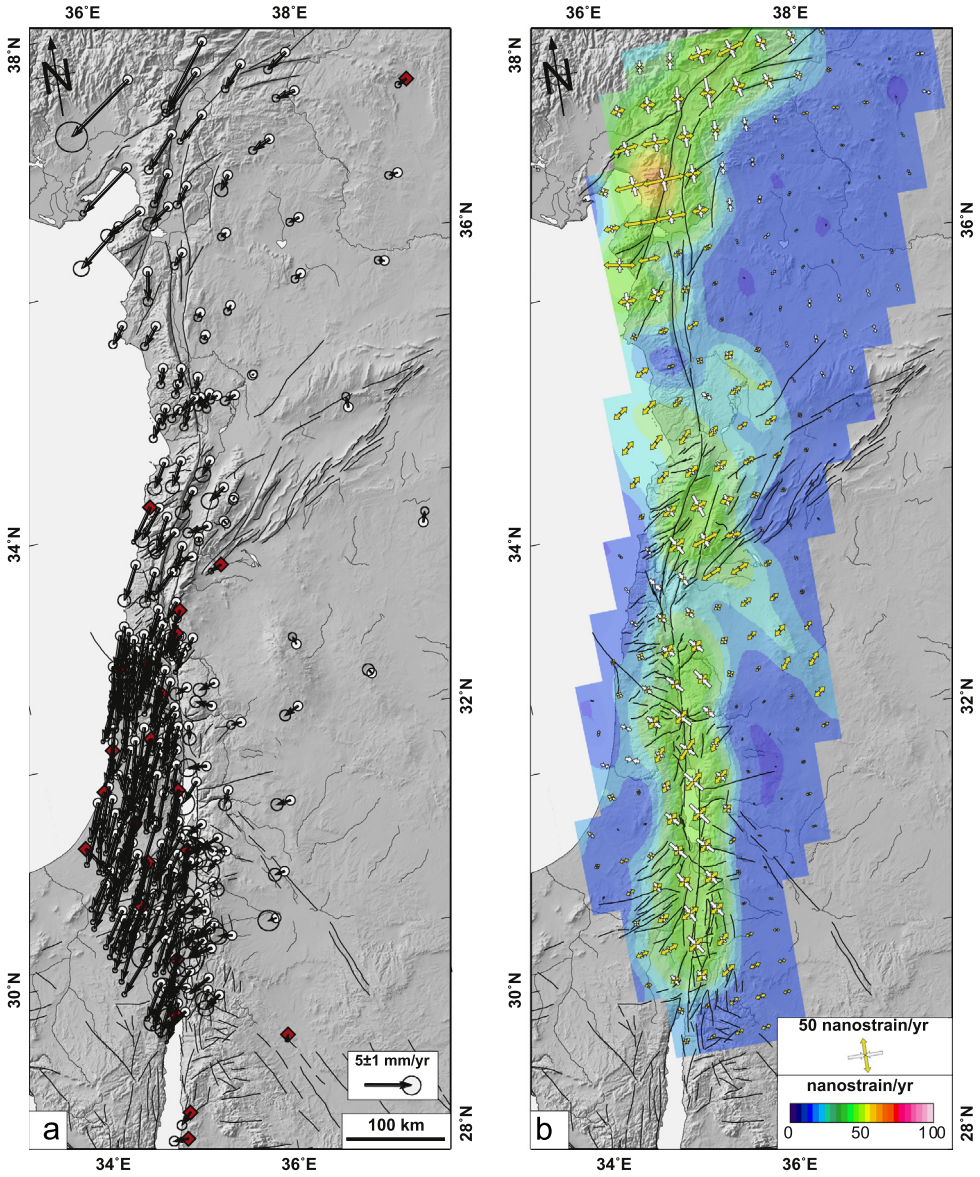

Fig. 5. (a) GPS velocities and 1–σ associated errors in a fixed Arabian plate (see Table 1 for more details). (b) Geodetic strain-rate parameters: the colour in the background shows the magnitude of the maximum shear strain-rate, while arrows represent the greatest extensional (yellow) and contractional (white) horizontal strain-rates. (For interpretation of the references to colour in this figure legend, the reader is referred to the web version of this article.)

By taking into account the method described in Beavan and Haines (2001), we computed the 2D strain-rate tensor and associated uncertainties over the studied area. As a first step, by using a bicubic spline interpolation, we interpolated the observed GPS velocity field and the associated covariance information on a regular $0.3^\circ \times 0.3^\circ$ grid whose nodes do not coincide with any of the GPS stations and which extends from 33.90° to 39.60° in longitude East and from 28.80° to 38.10° in latitude North. As a final step, we computed the average 2D strain-rate tensor as a derivative of the velocities at the centre of each grid cell. The estimated strain-rates are shown in Fig. 5b: the arrows show the greatest extensional (ε_{Hmax}) and contractional (ε_{hmin}) horizontal strain-rates, whereas the colour scale in the background shows the magnitude of the maximum shear strain-rate. The northern part of the investigated area, encompassing the entire DSFS–EAF–Bitlis–Zagros junction, is characterized by high strain-rate values (up to ~85 nanostrain/yr) with ε_{hmin} axes prevailing N–S oriented, coupled with ε_{Hmax} E–W oriented (Fig. 5b). Southward, the ε_{hmin} axes are prevailing NW–SE oriented along the DSFS with the exception of the PFB, where ε_{hmin} values (up to ~50 nanostrain/yr) show a fan-shaped feature with axes rotating eastward to a N–S attitude and sharply decreasing in magnitude (Fig. 5b). Along this area, the strain-rate is characterized by values up to ~50 nanostrain/yr, increasing up to ~80 nanostrain/yr southward in the area comprised between the Dead Sea and the Gulf of Aqaba. Regarding the maximum shear strain-rate, the "warm" colour (*i.e.* higher values) regions of Fig. 5b clearly follow the DSFS, indicating that much of the deformation is accommodated in a narrow region along the fault system itself.

5. Comparison between stress and strain-rate fields

Considering stress data obtained in this study and all available data reported in literature and in the World Stress Map project, we have compiled a multidisciplinary dataset of 33 horizontal stress indicators (see Table S3 of the "Supplementary material" section

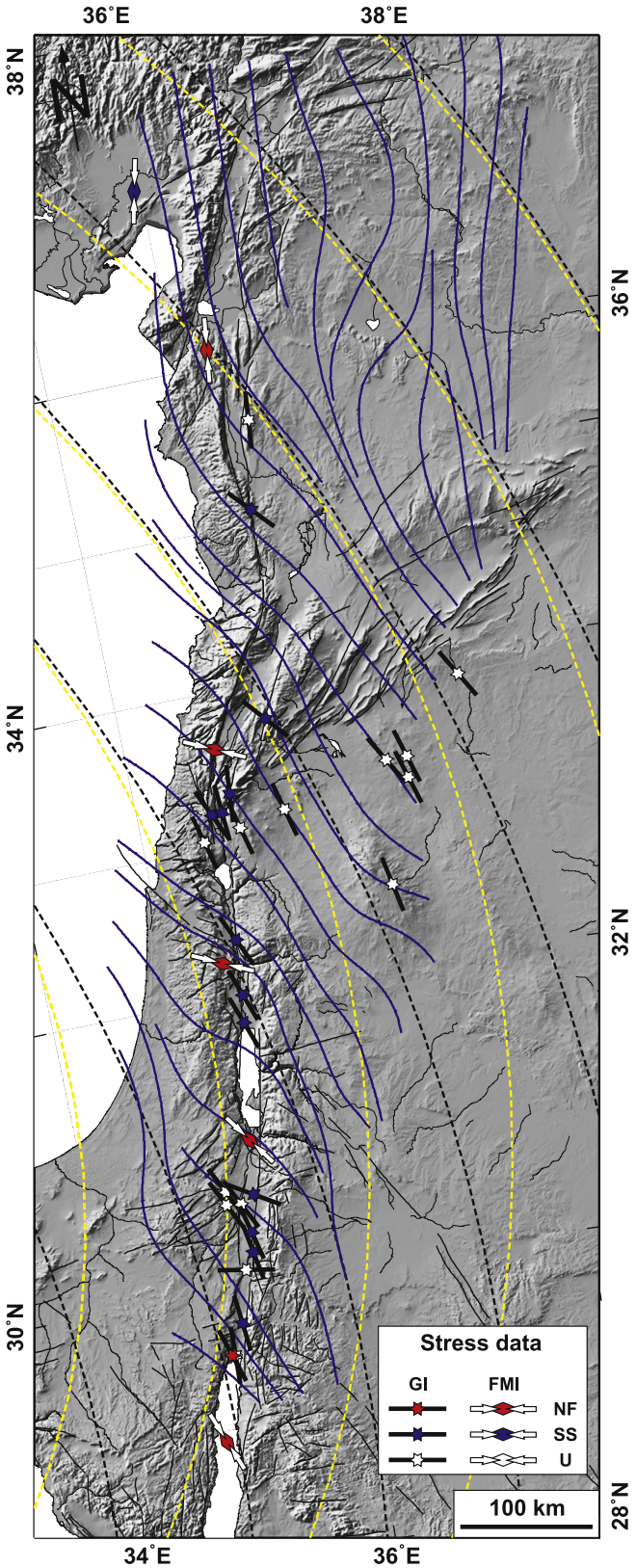

Fig. 6. Map of the S_{Hmax} inferred from geological indicators (GI) and from the inversion of FPSs performed in this study. See Table S3 of the "Supplementary material" section for additional details. The trajectories for maximum contractional (ε_{hmin}) horizontal strain-rate are reported as continuous curved lines in blue. Dashed lines draw the expected Eurasia–Arabia (black lines) and Nubia–Arabia relative motion direction (yellow lines). (For interpretation of the references to colour in this figure legend, the reader is referred to the web version of this article.)

for details), classified according to the quality ranking system described in Zoback (1992).

The present-day, regional stress field of the investigated area, in terms of S_{Hmax} orientation, is shown in Fig. 6. Stress data are spatially non-uniformly distributed along the DSFS, covering the southern and central sectors of the fault system with good detail, and spanning the 0–20 km depth interval, sampling the whole upper crust. Of course, density of data is inadequate to resolve the pattern of vertical stress deviations at any given sector. Although the S_{Hmax} orientations are computed from different techniques, in the investigated area they yield consistent orientations despite the different depths and volumes of rock sampled. In addition, the stress pattern is reconstructed from results that cover a variety of time spans, from a few years or decades (FPSs) to Pleistocene age (geological observations). This last aspect highlights that at least in the investigated area the maximum compressive stress has maintained the same orientations since the Pleistocene.

In the northern part of the investigated area the present-day stress field is sampled by very few data (FM01, FM02 and WSM-021) showing a prevailing N–S attitude, which is in agreement with the NNW–SSE orientations obtained by Yilmaz et al. (2006) for the central sector of EAF (northern edge of the area mapped in Fig. 6), through the inversion of slip vectors measured on strike-slip faults affecting Neocene and Quaternary deposits as well as Mesozoic bedrocks. The stress field is characterized by a transtensional strike-slip faulting regime (FM01 stress indicator; $R=0.63$) close to the EAF and by a normal faulting stress regime southward at the Hatay triple junction. Indeed, the FM02 stress indicator shows an R-value of 0.92, which indicates the coexistence of a normal faulting stress regime with a strike-slip one.

Both in the central and in the southern parts of the DSFS, the S_{Hmax} pattern exhibits a relatively uniform NNW–SSE orientation that is at approximately 30–45° to the average strike of the fault system. Few stress indicators show an angle larger than 70° between the S_{Hmax} orientation and the DSFS (see FM03 and GS-002 along its restraining bend and FM04, GS-001 and WSM-009 along its central sector in Fig. 6). The stress field is characterized by a normal faulting stress regime but with generally high R-values, indicating even now the coexistence of a normal faulting stress regime and a strike-slip one. South of the PFB, the stress field is sampled by some geological indicators and exhibits a NNW–SSE orientation, very similar to the one observed along the central sector of the DSFS.

To investigate the spatial pattern of stress and strain-rate fields, we computed a trajectory map for the minimum contractional (ε_{hmin}) horizontal strain-rates orientation using a smoothing algorithm (Palano et al., 2011). The simple visual comparison between the S_{Hmax} and the ε_{hmin} directions reveals that both orientations are near-parallel (Fig. 6), indicating that in the investigated area the crust is shortening in the direction of maximum compression (or extending in the direction of least compression S_{hmin}). Roughly speaking, in the perfectly elastic case, if strain and stress fields are related to the same process, we should observe that strain and stress axes were parallel. Moreover, in the anisotropic and inhomogeneous case (as a brittle deformed heterogeneous crust), strain and stress may have an oblique relationship (see Palano et al. (2013) and references therein for an overview). In addition, it must be noted that we compare stresses at depth with strain-rates observed at the Earth's surface; hence, we may expect some differences if there is a depth dependence of the processes causing the stress and strain-rate fields. Indeed, some local angular discrepancies between the S_{Hmax} and the ε_{hmin} directions can be recognized (*i.e.* along the DSFS restraining bend); however, the current density of data is inadequate to investigate them deeply.

In the following, we analyzed the strain–stress angular relationship with respect to the regional predicted directions of

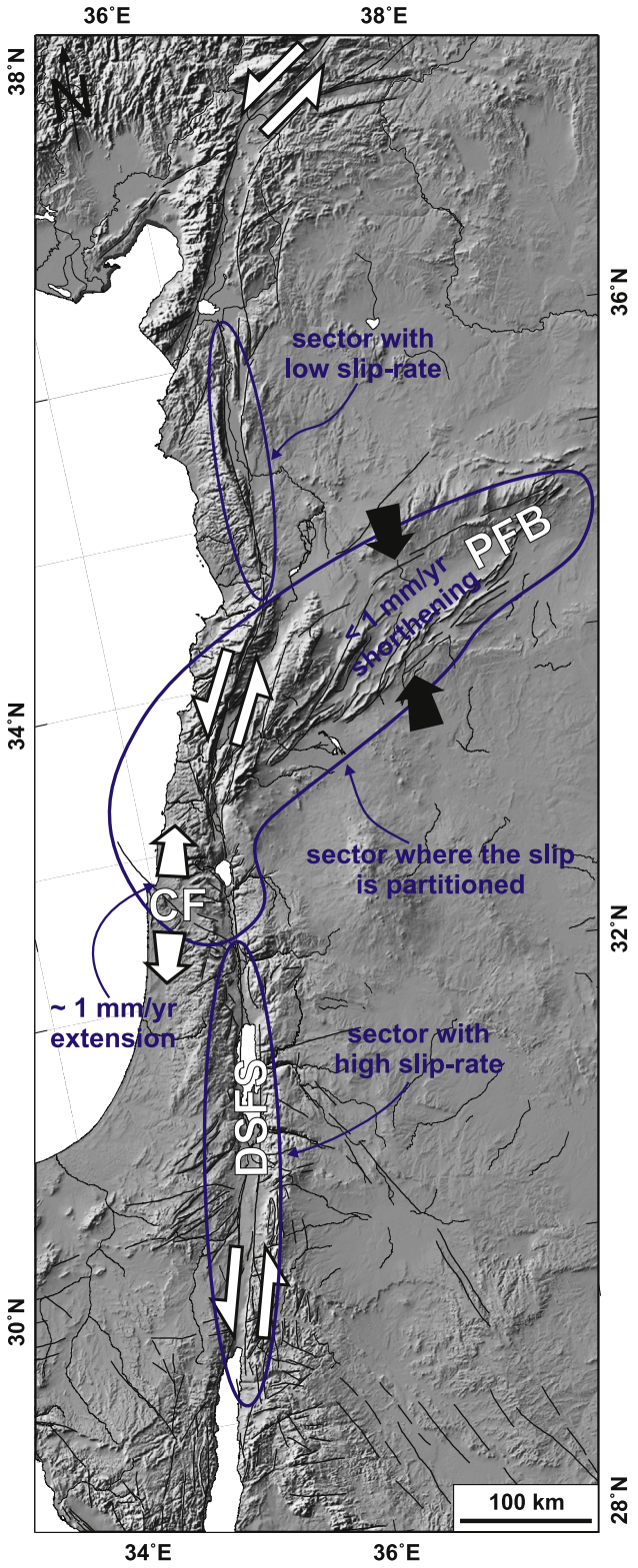

Fig. 7. Schematic model illustrating the slip-partition between the Arabian and Sinai plates, resulting in a northward decrease in motion of Arabia relative to Eurasia. In detail, part of this slip is partitioned as active shortening (less than 1 mm/yr) along the PFB and as active extension (~1.0 mm/yr) across the Carmel fault.

motion of Arabia relative to the Nubian and Eurasian plates (small circles around their poles of rotation; Fig. 6). The visual inspection reveals that in the central and southern sectors of DSFS the strain–stress pattern matches well with the predicted motion of Arabia relative to the Eurasian plate (black dashed trajectories in Fig. 6), while considering the predicted motion of Arabia relative to the Nubian plate (yellow dashed trajectories in Fig. 6) the agreement is limited only to the central sector of DSFS. Furthermore, in the northern sector of DSFS, the stress–strain pattern shows a clockwise rotation of about 40° with respect to both the Eurasia–Arabia and Nubia–Arabia predicted motion patterns.

The general azimuthal consistency over a large part of the investigated area suggests that the observed stress–strain pattern reflects to first-order the motion of the Arabian plate relative to Eurasia. In the northern sector of the DSFS, the observed stress–strain pattern may largely be related to the complex tectonic interaction between different plates and blocks (*i.e.* Arabia, Eurasia, Nubia, Sinai and Anatolia) along the Hatay triple junction and/or simply related to an upper-lithosphere extension in roughly an E–W direction (as observed from FM01 and FM02 stress data) in response to a flexure of the lithosphere along the N–S direction as shown by Sagy et al. (2003).

6. Discussion and conclusion

Here we have focused on the current geodetic velocities, strain-rate and stress fields across the DSFS by using GPS data (coming from recent continuously operating stations and published results) and tectonic stress information (provided by earthquake focal mechanisms and geological data). To depict a clear description of the ongoing active processes over the investigated area, in the following we discuss our results with respect to previous findings available in recent literature.

6.1. Geodetic velocity and slip-rate variations along the DSFS

GPS measurements carried out on different sectors of the DSFS, aligned to different reference frames, have provided the first order geodetic velocity around the fault system (Le Beon et al., 2008; Alchalbi et al., 2010; ArRajehi et al., 2010; Al Tarazi et al., 2011). By using 1-D elastic dislocation models (*e.g.* Savage and Burford, 1973), these authors observed some slip-rate variations among the different sectors of the DSFS and have highlighted how these variations are generally in agreement with the long-term geological estimations. Here, we report the updated velocity field computed from new observations and earlier published data and referred to a fixed Arabian plate (Table 1) in the ITRF2008 reference frame, based on a better data distribution.

This updated geodetic velocity field well depicts the general left-lateral motion of the DSFS. As mentioned above, this velocity field reveals some differences in slip-rate pattern between the northern and the southern sectors of the DSFS, evidencing how the southern sector of the fault system is characterized by higher slip-rate values. In greater detail, the northern sector of DSFS is characterized by a SSW-directed velocity field with motions passing from ~7.5 mm/yr along the Kara Su Valley (mainly related to the ongoing tectonic activity on the Hatay triple junction) to ~1.8 mm/yr at the southern end of the Ghab Valley. The central sector of DSFS is characterized by velocities of ~3.5 mm/yr westward of the Yammouneh fault gradually passing to values of ~0.2 mm/yr eastward of the Serghaya fault, evidencing the partitioning of the general left-lateral motion into the different segments of the DSFS. The southern sector of DSFS is characterized by a gradual increase in velocity values (at a rate of ~0.07 mm/yr per km), passing from values of ~2.9 mm/yr south of PFB to ~5.0 mm/yr close to the Gulf of Aqaba

Geodetic estimations, based on two stations installed across the PFB, have inferred less than 1 mm/yr of active regional shortening along the NNW–SSE direction (Alchalbi et al., 2010). Active shortening

across the PFB, based on historical seismicity and evidences of Late Quaternary deformation, has been suggested by several authors (Chaimov et al., 1990; Salamon et al., 1996; Abou Romieh et al., 2009). Furthermore, Sadeh et al. (2012), by using a dense GPS network, detected an oblique motion along the Carmel fault with ~0.7 mm/yr left-lateral and ~0.6 mm/yr extension. These estimations suggest how part of the present-day left-lateral motion between the Arabian and the Sinai plates could be adsorbed as active shortening along the PFB and as active extension across the Carmel fault (Fig. 7). This aspect is in good agreement with the observed widespread pattern of instrumental seismicity over the area where the slip distribution occurs.

6.2. Stress and strain-rate fields

We investigated the current stress field along the DSFS through the analyses of new data (earthquake focal mechanisms) and published data (geological data). The inversion for stress tensor of earthquake focal mechanisms occurring along the DSFS allows detecting a stress regime characterized by an always subhorizontal $\sigma 3$, with $\sigma 2$ and $\sigma 1$ very close in magnitude. This aspect highlights how along the DSFS there are both a strike-slip faulting stress regime and a normal one in agreement with previous findings. For instance, Salamon et al. (2003) by using seismological data highlighted how the left-lateral shear characterizes the whole DSFS as does the normal regime, which reflects the extensional component of the fault system. Bowman et al. (2003) have shown that oblique motion at depth tends to splay near the surface due to the propagation of lobes of strain concentration and their interaction with the free surface, encouraging the partitioning to normal, thrust and strike slip faulting. Following this model, Deves et al. (2011) have shown that along the Dead Sea region, the oblique motion from the DSFS at depth breaks down near the surface to "multiple mechanisms", namely dip-slip and strike-slip. In such model, the principal axes of stress field can rotate rapidly in space and time, thus, local stress indicators (*i.e.* FPSs, borehole breakouts, etc.) orthogonally oriented with respect to the fault strike (see for example GS-001, GS-002, FM03, FM04 WSM-009 stress data in Fig. 6 which show a larger than 70° angle with respect to the DSFS), do not require the main fault itself to experience abnormal stress conditions when it slips as instead observed along a large sector of the San Andreas fault (Townend and Zoback, 2004).

Taking into account the general S_{Hmax} orientation pattern, we observe a marked azimuthal difference between the southern-central sector of the DSFS and the northern one. In the southern–central part of the DSFS, the S_{Hmax} pattern exhibits a relatively uniform NNW–SSE orientation in good agreement with the predicted regional directions of motion of Arabia relative to the Eurasian plate. In the northern sector of the DSFS, the azimuthal stress pattern shows a prevailing N–S attitude with a clockwise rotation of about 40° with respect to the predicted regional directions of motion. The visual comparison between the stress and the strain-rate azimuthal patterns reveals that both orientations are near-parallel, indicating that present-day stress and ground deformation patterns are primarily driven by the same tectonic processes. For instance, Chang et al. (2003) and Keiding et al. (2009) on investigating the S_{Hmax} and ε_{hmin} patterns in Iceland and in Taiwan, respectively, have found a remarkable azimuthal agreement between the two patterns and have evidenced that both are primarily driven by forces arising from plate motion. Moreover, Townend and Zoback (2006) highlighted how the S_{Hmax} directions in Japan concurred well with the direction of ε_{hmin} only after the effects of interseismic subduction thrust locking had been subtracted from geodetic observations.

In our case, since in the southern and central sectors of the DSFS the S_{Hmax} and ε_{hmin} azimuthal patterns are aligned to the Eurasia–Arabia convergence motion, we retain that the largest component of the observed strain–stress fields is given by the plate-driving forces related to this convergence instead of the shear between Nubia and Arabia plates. This aspect is consistent with the findings of ArRajehi et al. (2010) who hypothesized that the Arabia plate motion is primarily driven by the negative buoyancy of the subducted ocean lithosphere (*i.e.* slab pull) beneath the Bitlis–Zagros fold-thrust belt and subordinately by the rifting along the Red Sea–Gulf of Aden region.

In the northern sector of the DSFS, the observed stress–strain fields show an oblique azimuthal relationship with respect to the regional Eurasia–Arabia convergence motion. We retain that here, the stress field may be related to the complex tectonic interaction between the Arabian, Eurasian and African/Sinai plates which occurs along the Hatay triple junction and/or to an upper-lithosphere extension in the E–W direction in response to a flexure of the lithosphere along the N–S direction as evidenced in Sagy et al. (2003). Unfortunately, the limited number of stress observations on this area does not allow to adequately tackle these questions.

Addressing these questions through the use of simple elastic dislocation models and/or more complex approaches such as the "Finite Element Method" could be a principal objective of future studies. In addition, further geodetic and seismological observations will improve the spatial density of the stress/strain resolution, allowing to resolve the regional pattern of stress distribution in depth.

Acknowledgements

We thank Amotz Agnon and Luigi Ferranti for their critical reviews and constructive comments that greatly improved the paper. We greatly appreciated the suggestions by the editor Peter Shearer. We express our gratitude to Damien Delvaux for making his WinTensor program available for the stress inversion and to Flavio Cannavò for helping us with the strain trajectories computation. We thank Stephen Conway for correcting and improving the English language of this manuscript. Luca Manzella contributed to the preliminary analysis of data. GMT software was used to create all figures.

Appendix A. Supplementary material

Supplementary data associated with this article can be found in the online version at http://dx.doi.org/10.1016/j.epsl.2013.03.043.

References

Abdul-Wahed, M.K., Al-Tahhan, I., 2010. Preliminary outline of the seismologically active zones in Syria. Ann. Geophys. 53 (4), 1–9, http://dx.doi.org/10.4401/ag-4683.

Abou Romieh, M., Westaway, R., Daoud, M., Radwan, Y., Yassminh, R., Khalil, A., Al-Ashkar, A., Loughlin, S., Arrell, K., Bridgland, D., 2009. Active crustal shortening in NE Syria revealed by deformed terraces of the River Euphrates. Terra Nova 21 (6), 427–437, http://dx.doi.org/10.1111/j.1365-3121.2009.00896.x.

Agnon, A., Migowski, C., Marco, S., 2006. Intraclast breccias in laminated sequences reviewed: recorders of paleo-earthquakes. In: Enzel, Y., Agnon, A., Stein, M. (Eds.), New Frontiers in Dead Sea Paleoenvironmental Research. Geological Society of America Special Paper 401, pp. 195–214, http://dx.doi.org/10.1130/2006.2401(1113).

Al Tarazi, E., Abu-Rajab, J., Gomez, F., Cochran, W., Jaafar, R., Ferry, M., 2011. GPS measurements of near-field deformation along the southern Dead Sea Fault System. Geochem. Geophys. Geosyst. 12, Q12021, http://dx.doi.org/10.1029/2011GC003736.

Alchalbi, A., Daoud, M., Gomez, F., McClusky, S., Reilinger, R., Romeyeh, M.A., Alsouod, A., Yassminh, R., Ballani, B., Darawcheh, R., Sbeinati, R., Radwan, Y., Masri, R.A., Bayerly, M., Ghazzi, R.A., Barazangi, M., 2010. Crustal deformation in northwestern Arabia from GPS measurements in Syria: slow slip rate along the northern Dead Sea Fault. Geophys. J. Int. 180, 125–135, http://dx.doi.org/10.1111/j.1365-246X.2009.04431.x.

Aldersons, F., Ben-Avraham, Z., Hofstetter, A., Kissling, E., Al-Yazjeen, T., 2003. Lower-crustal strength under the Dead Sea basin from local earthquake data and rheological modeling. Earth Planet. Sci. Lett. 214 (1–2), 129–142, http://dx.doi.org/10.1016/S0012-821X(03)00381-9.

Ambraseys, N.N., Jackson, J.A., 1998. Faulting associated with historical and recent earthquakes in the Eastern Mediterranean region. Geophys. J. Int. 133, 390–406, http://dx.doi.org/10.1046/j.1365-246X.1998.00508.x.

Ambraseys, N.N., Melville, C.P., Adams, R.D., 1994. The Seismicity of Egypt, Arabia and the Red Sea: A Historical Review. Cambridge University Press, Cambridge, UK, 1–181, http://dx.doi.org/10.1017/CBO9780511524912.

ArRajehi, A., McClusky, S., Reilinger, R., Daoud, M., Alchalbi, A., Ergintav, S., Gomez, F., Sholan, J., Bou-Rabee, F., Ogubazghi, G., Haileab, B., Fisseha, S., Asfaw, L., Mahmoud, S., Rayan, A., Bendik, R., Kogan, L., 2010. Geodetic constraints on present-day motion of the Arabian Plate: implications for Red Sea and Gulf of Aden rifting. Tectonics 29, TC3011, http://dx.doi.org/10.1029/2009TC002482.

Arvidsson, R., Ben-Avraham, Z., Ekström, G., Wdowinski, S., 1998. Plate tectonic framework for the October 9, 1996, Cyprus earthquake. Geophys. Res. Lett. 25 (12), 2241–2244, http://dx.doi.org/10.1029/98GL01547.

Bartov, Y., Steinitz, G., Eyal, M., Eyal, Y., 1980. Sinistral movement along the Gulf of Aqaba—its age and relation to the opening of the Red Sea. Nature 285, 220–221.

Beavan, J., Haines, J., 2001. Contemporary horizontal velocity and strain rate fields of the Pacific–Australian plate boundary zone through New Zealand. J. Geophys. Res. 106, 741–770, http://dx.doi.org/10.1029/2000JB900302.

Bott, M.H.P., 1959. The mechanisms of oblique slip faulting. Geol. Mag. 96, 109–117.

Bowman, D., King, G., Tapponnier, P., 2003. Slip partitioning by elasto-plastic propagation of oblique slip at depth. Science 300, 1121–1123, http://dx.doi.org/10.1126/science.1082180.

Braunmiller, J., Kradolfer, U., Baer, M., Giardini, D., 2002. Regional moment tensor determination in the European–Mediterranean area—initial results. Tectonophysics 356, 5–22, http://dx.doi.org/10.1016/S0040-1951(02)00374-8.

Chaimov, T.A., Barazangi, M., Al-Saad, D., Sawaf, T., Gebran, A., 1990. Crustal shortening in the Palmyride fold belt, Syria, and implications for movement along the Dead Sea Fault System. Tectonics 9, 1369–1386, http://dx.doi.org/10.1029/TC009i006p01369.

Chang, C.P., Chang, T.Y., Angelier, J., Kao, H., Lee, J.C., Yu, S.B., 2003. Strain and stress field in Taiwan oblique convergent system: constraints from GPS observation and tectonic data. Earth Planet. Sci. Lett. 214 (1–2), 115–127, http://dx.doi.org/10.1016/S0012-821X(03)00360-1.

Daëron, M., Benedetti, L., Tapponnier, P., Sursock, A., Finkel, R., 2004. Constraints on the post 25-ka slip rate of the Yammouneh fault (Lebanon) using *in-situ* cosmogenic Cl36 dating of offset limestone-clast fans. Earth Planet. Sci. Lett. 227, 105–119, http://dx.doi.org/10.1016/j.epsl.2004.07.014.

Delvaux, D., 2012. Release of program Win-Tensor 4.0 for tectonic stress inversion: statistical expression of stress parameters. Geophysical Research Abstracts 14, EGU2012-5899, EGU General Assembly, Vienna.

Delvaux, D., Barth, A., 2010. African stress pattern from formal inversion of focal mechanism data. Tectonophysics 482 (1–4), 105–128, http://dx.doi.org/10.1016/j.tecto.2009.05.009.

Delvaux, D., Sperner, B., 2003. Stress tensor inversion from fault kinematic indicators and focal mechanism data: the TENSOR program. In: Nieuwland, D. (Ed.), New Insights into Structural Interpretation and Modelling, 212. Geological Society, London, Special Publication, pp. 75–100.

Deves, M., King, G.C.P., Klinger, Y., Agnon, A., 2011. Localised and distributed deformation in the Lithosphere: modelling the Dead Sea region in 3 dimensions. Earth Planet. Sci. Lett. 308, 172–184, http://dx.doi.org/10.1016/j.epsl.2011.05.044.

Dziewonski, A.M., Woodhouse, J.H., 1983. An experiment in the systematic study of global seismicity: centroid moment-tensor solutions for 201 moderate and large earthquakes of 1981. J. Geophys. Res. 88, 3247–3271, http://dx.doi.org/10.1029/JB088iB04p03247.

Dziewonski, A.M., Chou, T.A., Woodhouse, J., 1981. Determination of earthquake source parameters from waveform data for studies of global and regional seismicity. J. Geophys. Res. 86, 2825–2852, http://dx.doi.org/10.1029/JB086iB04p02825.

Elenean, K.M.A., Aldamegh, K.S., Zharan, H.M., Hussein, H.M., 2009. Regional waveform inversion of 2004 February 11 and 2007 February 09 Dead Sea earthquakes. Geophys. J. Int. 176 (1), 185–199, http://dx.doi.org/10.1111/j.1365-246X.2008.03971.x.

Elias, A., Tapponnier, P., Singh, S.C., King, G.C.P., Briais, A., Daëron, M., Carton, H., Sursock, A., Jacques, E., Jomaa, R., Klinger, Y., 2007. Active thrusting offshore Mount Lebanon: source of the tsunamigenic A.D. 551 Beirut–Tripoli earthquake. Geology 35, 755–758, http://dx.doi.org/10.1130/G23631A.1.

Ellenblum, R., Marco, S., Agnon, A., Rockwell, T., Boas, A., 1998. Crusader castle torn apart by earthquake at dawn, 20 May 1202. Geology 26 (4), 303–306, http://dx.doi.org/10.1130/0091-7613(1998)026<0303:CCTABE>2.3.CO;2.

Eyal, M., Eyal, Y., Bartov, Y., Steinitz, G., 1981. The tectonic development of the western margin of the Gulf of Elat (Aqaba) Rift. Tectonophysics 80 (1–4), 39–66, http://dx.doi.org/10.1016/0040-951(81)90141-4.

Ferry, M., Meghraoui, M., Karaki, N.A., Al-Taj, M., Amoush, H., Al-Dhaisat, S., Barjous, M., 2007. A 48-kyr-long slip rate history for the Jordan Valley segment of the Dead Sea fault. Earth Planet. Sci. Lett. 260, 394–406, http://dx.doi.org/10.1016/j.epsl.2007.05.049.

Freund, R., Garfunkel, Z., Zak, I., Goldberg, M., Weisbrod, T., Derin, B., 1970. The shear along the Dead Sea rift. Philos. Trans. R. Soc. London (Ser. A) 267, 107–130, http://dx.doi.org/10.1098/rsta.1970.0027.

Frohlich, C., 1992. Triangle diagrams: ternary graphs to display similarity and diversity of earthquake focal mechanisms. Phys. Earth Planet. Inter. 75, 193–198, http://dx.doi.org/10.1016/0031-9201(92)90130-N.

Garfunkel, Z., 1981. Internal structure of the Dead Sea leaky transform (rift) in relation to plate kinematics. Tectonophysics 80, 81–108, http://dx.doi.org/10.1016/0040-1951(81)90143-8.

Garfunkel, Z., 1997. The history and formation of the Dead Sea basin in The Dead Sea, the lake and its setting. In: Niemi, T., Ben-Avraham, Z., Gat, J. (Eds.), Oxford Monographs on Geology and Geophysics 36. Oxford University Press, New York, USA.

Ginat, H., Enzel, T., Avni, Y., 1998. Translocated Plio-Pleistocene drainage systems along the Arava fault of the Dead Sea Transform. Tectonophysics 284, 151–160, http://dx.doi.org/10.1016/S0040-1951(97)00165-0.

Girdler, R.W., 1990. The Dead Sea transform fault system. Tectonophysics 180, 1–13, http://dx.doi.org/10.1016/0040-1951(90)90367-H.

Gomez, F., Meghraoui, M., Darkal, A.N., Hijazi, F., Mouty, M., Suleiman, Y., Sbeinati, R., Darawcheh, R., Al-Ghazzi, R., Barazangi, M., 2003. Holocene faulting and earthquake recurrence along the Serghaya branch of the Dead Sea fault system in Syria and Lebanon. Geophys. J. Int. 153, 1–17, http://dx.doi.org/10.1046/j.1365-246X.2003.01933.x.

Gomez, F., Karam, G., Khawlie, M., McClusky, S., Vernant, P., Reilinger, R., Jaafar, R., Tabet, C., Khair, K., Barazangi, M., 2007. Global Positioning System measurements of strain accumulation and slip transfer through the restraining bend along the Dead Sea fault system in Lebanon. Geophys. J. Int. 168, 1021–1028, http://dx.doi.org/10.1111/j.1365-246X.2006.03328.x.

Hempton, M.R., 1987. Constraints on Arabian plate motion and extensional history of the Red Sea. Tectonics 6, 687–705, http://dx.doi.org/10.1029/TC006i006p00687.

Herring, T.A., King, R.W., McClusky, S.C., 2010. Introduction to GAMIT/GLOBK, Release 10.4. Massachusetts Institute of Technology, Cambridge MA, pp. 1–48.

Hofstetter, A., Thio, H.K., Shamir, G., 2003. Source mechanism of the 22/11/1995 Gulf of Aqaba earthquake and its aftershock sequence. J. Seismol. 7 (1), 99–114, http://dx.doi.org/10.1023/A:1021206930730.

Hofstetter, R., Klinger, Y., Amrat, A.Q., Rivera, L., Dorbath, L., 2007. Stress tensor and focal mechanisms along the Dead Sea fault and related structural elements based on seismological data. Tectonophysics 429, 165–181, http://dx.doi.org/10.1016/j.tecto.2006.03.010.

Imprescia, P., Pondrelli, S., Vannucci, G., Gresta, S., 2012. Regional centroid moment tensor solutions in Cyprus from 1977 to the present and seismotectonic implications. J. Seismol. 16 (2), 147–167, http://dx.doi.org/10.1007/s10950-011-9254-7.

Imprescia, P., 2010. Meccanismi focali di terremoti come strumento per la definizione della sismotettonica dell'area mediterranea. Ph.D. Thesis. University of Catania.

Janssen, C., Hoffmann-Rothe, A., Bohnhoff, M., Wetzel, H.U., Matar, A., Khatib, M., 2007. Different styles of faulting deformation along the Dead Sea Transform and possible consequences for the recurrence of major earthquakes. J. Geodyn. 44, 66–89, http://dx.doi.org/10.1016/j.jog.2007.01.002.

Karabacak, V., Altunel, E., 2013. Evolution of the northern Dead Sea Fault Zone in southern Turkey. J. Geodyn. 65, 282–291, http://dx.doi.org/10.1016/j.jog.2012.04.012.

Keiding, M., Lund, B., Árnadóttir, T., 2009. Earthquakes, stress, and strain along an obliquely divergent plateboundary: Reykjanes Peninsula, southwest Iceland. J. Geophys. Res. 114, B09306, http://dx.doi.org/10.1029/2008JB006253.

Klinger, Y., Avouac, J.P., Abouh Karaki, N., Tisnerat, N., 2000. Seismic behaviour of the Dead Sea fault along Araba valley, Jordan. Geophys. J. Int. 142, 769–782, http://dx.doi.org/10.1046/j.1365-246x.2000.00166.x.

Kraeva, N., Hofstetter, A., Meirova, T., 2010. Waveform moment tensor inversion of earthquakes in Israel and adjacent regions. Isr. J. Earth Sci. 58, 177–192, http://dx.doi.org/10.1560/IJES.58.3-4.177.

Le Beon, M., Klinger, Y., Amrat, A.Q., Agnon, A., Dorbath, L., Baer, G., Ruegg, J.C., Charade, O., Mayyas, O., 2008. Slip rate and locking depth from GPS profiles across the southern Dead Sea Transform. J. Geophys. Res. 113, B11403, http://dx.doi.org/10.1029/2007JB005280.

Le Pichon, X., Gaulier, J.M., 1988. The rotation of Arabia and the Levant fault system. Tectonophysics 153, 271–294, http://dx.doi.org/10.1016/0040-1951(88)90020-0.

Lunina, O.V., Mart, Y., Gladkov, A.S., 2005. Fracturing patterns, stress fields and earthquakes in the Southern Dead Sea rift. J. Geodyn. 40, 216–234, http://dx.doi.org/10.1016/j.jog.2005.07.010.

Mahmoud, S., Reilinger, R., McClusky, S., Vernant, P., Tealeb, A., 2005. GPS evidence for northward motion of the Sinai Block: implications for E. Mediterranean tectonics. Earth Planet. Sci. Lett. 238, 217–224, http://dx.doi.org/10.1016/j.epsl.2005.06.063.

Mahmoud, Y., Masson, F., Meghraoui, M., Cakir, Z., Alchalbi, A., Yavasoglu, H., Yönlü, O., Daoud, M., Ergintav, S., Inan, S., 2013. Kinematic study at the junction of the East Anatolian fault and the Dead Sea fault from GPS measurements. J. Geodyn. 67, 30–39, http://dx.doi.org/10.1016/j.jog.2012.05.006.

Makovsky, Y., Wunch, A., Areily, R., Shaked, Y., Rivlin, A., Shemesh, A., Ben Avraham, Z., Agnon, A., 2008. Quaternary transform kinematics constrained by sequence stratigraphy and submerged coastline features: the Gulf of Aqaba. Earth Planet. Sci. Lett. 271, 109–122, http://dx.doi.org/10.1016/j.epsl.2008.03.057.

Marco, S., Rockwell, T., Heimann, A., Frieslander, U., Agnon, A., 2005. Late Holocene activity of the Dead Sea Transform revealed in 3D palaeoseismic trenches on the Jordan Gorge segment. Earth Planet. Sci. Lett. 234, 189–205, http://dx.doi.org/10.1016/j.epsl.2005.01.017.

Meghraoui, M., Cakir, Z., Masson, F., Mahmoud, Y., Ergintav, S., Alchalbi, A., Inan, S., Daoud, M., Yonlu, O., Altunel, E., 2011. Kinematic modelling at the triple junction between the Anatolian, Arabian, African plates (NW Syria and in SE Turkey). Geophysical Research Abstracts 13, EGU2011-12599, EGU General Assembly, Vienna.

Niemi, T.M., Zhang, H.W., Atallah, M., Harrison, J.B.J., 2001. Late Pleistocene and Holocene slip rate of the Northern Wadi Araba fault, Dead Sea Transform, Jordan. J. Seismol. 5 (3), 449–474, http://dx.doi.org/10.1023/A:1011487912054.
Nikolaidis, R., 2002. Observation of Geodetic and Seismic Deformation with the Global Positioning System. Ph.D. Thesis. University of California.
Palano, M., Rossi, M., Cannavò, C., Bruno, V., Aloisi, M., Pellegrino, D., Pulvirenti, M., Siligato, G., Mattia, M., 2010. Etn@ref, a geodetic reference frame for Mt. Etna GPS networks. Ann. Geophys. 53 (4), 48–79, http://dx.doi.org/10.4401/ag-4879.
Palano, M., Cannavò, F., Ferranti, L., Mattia, M., Mazzella, E., 2011. Strain and stress fields in the Southern Apennines (Italy) constrained by geodetic, seismological and borehole data. Geophys. J. Int. 187 (3), 1270–1282, http://dx.doi.org/10.1111/j.1365-246X.2011.05234.x.
Palano, M., Gonzalez, P., Fernandez, J., 2013. Strain and stress fields along the Gibraltar Orogenic Arc: constraints on active geodynamics. Gondwana Res. 23, 1071–1088, http://dx.doi.org/10.1016/j.gr.2012.05.021.
Pondrelli, S., Salimbeni, S., Morelli, A., Ekström, G., Postpischl, L., Vannucci, G., Boschi, E., 2011. European–Mediterranean Regional Centroid Moment Tensor catalog: solutions for 2005–2008. Phys. Earth Planet. Inter. 185 (3–4), 74–81, http://dx.doi.org/10.1016/j.pepi.2011.01.007.
Quennell, A.M., 1958. The structural and geomorphic evolution of the Dead Sea rift. Quart. J. Geol. Soc. 114, 1–24, http://dx.doi.org/10.1144/gsjgs.114.1.0001.
Reilinger, R., McClusky, S., Vernant, P., Lawrence, S., Ergintav, S., Cakmak, R., Ozener, H., Kadirov, F., Guliev, I., Stepanyan, R., Nadariya, M., Hahubia, G., Mahmoud, S., Sakr, K., ArRajehi, A., Paradissis, D., Al-Aydrus, A., Prilepin, M., Guseva, T., Evren, E., Dmitrotsa, A., Filikov, S.V., Gomez, F., Al-Ghazzi, R., Karam, G., 2006. GPS constraints on continental deformation in the Africa–Arabia–Eurasia continental collision zone and implications for the dynamics of plate interactions. J. Geophys. Res. 111, B05411, http://dx.doi.org/10.1029/2005JB004051.
Sadeh, M., Hamiel, Y., Ziv, A., Bock, Y., Fang, P., Wdowinski, S., 2012. Crustal deformation along the Dead Sea Transform and the Carmel Fault inferred from 12 years of GPS measurements. J. Geophys. Res. 117, B08410, http://dx.doi.org/10.1029/2012JB009241.
Sagy, A., Reches, Z., Agnon, A., 2003. Hierarchic three-dimensional structure and slip partitioning in the western Dead Sea pull-apart. Tectonics 22 (1), 1004, http://dx.doi.org/10.1029/2001TC001323.
Salamon, A., Hofstetter, A., Garfunkel, Z., Ron, H., 1996. Seismicity of the eastern Mediterranean region: perspective from the Sinai subplate. Tectonophysics 263, 293–305, http://dx.doi.org/10.1016/S0040-1951(96)00030-3.
Salamon, A., Hofstetter, A., Garfunkel, Z., Hagai Ron, R., 2003. Seismotectonics of the Sinai subplate—the eastern Mediterranean region. Geophys. J. Int. 155, 149–173, http://dx.doi.org/10.1046/j.1365-246X.2003.02017.x.
Savage, J.C., Burford, R.O., 1973. Geodetic determination of relative plate motion in central California. J. Geophys. Res. 78, 832–845, http://dx.doi.org/10.1029/JB078i005p00832.
Sbeinati, M.R., Darawcheh, R., Mouty, M., 2005. The historical earthquakes of Syria: an analysis of large and moderate earthquakes from 1365 BC to 1900 AD. Ann. Geophys. 48 (3), 347–435, http://dx.doi.org/10.4401/ag-3206.
Searle, M.P., Chung, S.L., Lo, C.H., 2010. Geological offsets and age constraints along the northern Dead Sea Fault, Syria. J. Geol. Soc. London 167, 1001–1008, http://dx.doi.org/10.1144/0016-76492010-009.
Shamir, G., 2006. The active structure of the Dead Sea Depression. In: Enzel Y., et al. (Eds.), New Frontiers in Paleoenvironmental Research. Geological Society of America Special Paper 40, pp. 15–32, http://dx.doi.org/10.1130/2006.2401(02).
Townend, J., Zoback, M.D., 2004. Regional tectonic stress near the San Andreas fault in central and southern California. Geophys. Res. Lett. 31, L15S11, http://dx.doi.org/10.1029/2003GL018918.
Townend, J., Zoback, M.D., 2006. Stress, strain, and mountain building in central Japan. J. Geophys. Res. 111 (3), http://dx.doi.org/10.1029/2005JB003759.
Vannucci, G., Gasperini, P., 2003. A database of revised fault plane solutions for Italy and surrounding regions. Comput. Geosci. 29 (7), 903–909, http://dx.doi.org/10.1016/S0098-3004(03)00094-3.
Vannucci, G., Gasperini, P., 2004. The new release of the database of Earthquake Mechanisms of the Mediterranean Area (EMMA Version 2). Ann. Geophys. 47 (1S), 307–334.
Vannucci, G., Imprescia, P., Gasperini, P., 2010. A new release (3.1) of the database of Earthquake Mechanisms of the Mediterranean Area (EMMA). ESC, 32nd General Assembly, September 6–10, Montpellier, France.
Walley, C.D., 1988. A braided strike-slip model for the northern continuation of the Dead Sea fault, and its implications to Levantine tectonics. Tectonophysics 145, 63–72, http://dx.doi.org/10.1016/0040-1951(88)90316-2.
Weber, M., Abu-Ayyash, K., Abueladas, A., Agnon, A., Alasonati Tasárová, Z., Al-Zubi, H., Babeyko, A., Bartov, Y., Bauer, K., Becken, M., Bedrosia, P.A., Ben-Avraham, Z., Bock, G., Bohnhoff, M., Bribach, J., Dulski, P., Ebbing, J., El-Kelani, R., Förster, A., Förster, H.-J., Frieslander, U., Garfunkel, Z., Goetze, H.J., Haak, V., Haberland, C., Hassouneh, M., Helwig, S., Hofstetter, A., Hoffmann-Rothe, A., Jäckel, K.H., Janssen, C., Jaser, D., Kesten, D., Khatib, M., Kind, R., Koch, O., Koulakov, I., Laske, G., Maercklin, N., Masarweh, R., Masri, A., Matar, A., Mechie, J., Meqbel, N., Plessen, B., Möller, P., Mohsen, A., Oberhänsli, R., Oreshin, S., Petrunin, A.G., Qabbani, I., Rabba, I., Ritter, O., Romer, R.L., Rümpker, G., Rybakov, M., Ryberg, T., Saul, J., Scherbaum, F., Schmidt, S., Schulze, A., Sobolev, S.V., Stiller, M., Stromeyer, D., Tarawneh, K., Trela, C., Weckmann, U., Wetzel, H.U., Wylegalla, K., 2009. Anatomy of the Dead Sea Transform from lithospheric to microscopic scale. Rev. Geophys. 47, RG2002, http://dx.doi.org/10.1029/2008RG000264.
Yilmaz, H., Over, S., Ozden, S., 2006. Kinematics of the East Anatolian Fault Zone between Turkoglu (Kahramanmaras) and Celikhan (Adiyaman), eastern Turkey. Earth Planets Space 58, 1463–1473.
Zoback, M.L., 1992. First- and second-order patterns of stress in the lithosphere: the World Stress Map Project. J. Geophys. Res. 97 (B8), 11703–11728.